Virtual Fixture Assistance for Suturing in Robot-Aided Pediatric Endoscopic Surgery

Murilo M. Marinho*, *Member, IEEE,* Hisashi Ishida*, Kanako Harada, *Member, IEEE,* Kyoichi Deie, and Mamoru Mitsuishi, *Member, IEEE*

Abstract—The limited workspace in pediatric endoscopic surgery makes surgical suturing one of the most difficult tasks. During suturing, surgeons have to prevent collisions between instruments and also collisions with the surrounding tissues. Surgical robots have been shown to be effective in adult laparoscopy, but assistance for suturing in constrained workspaces has not been yet fully explored. In this letter, we propose guidance virtual fixtures to enhance the performance and the safety of suturing while generating the required task constraints using constrained optimization and Cartesian force feedback. We propose two guidance methods: looping virtual fixtures and a trajectory guidance cylinder, that are based on dynamic geometric elements. In simulations and experiments with a physical robot, we show that the proposed methods increase precision and safety *in-vitro*.

Index Terms—Medical Robots and Systems, Kinematics, Collision Avoidance

I. INTRODUCTION

PEDIATRIC ENDOSCOPIC SURGERY for infants (<1 year old) and neonates has additional difficulties when compared with adult endoscopic surgery. For example, the workspace is narrower, often being described by medical doctors as "golf-ball sized". Constrained workspaces can be defined as having a volume of 200 cm^3 or less [1], which includes pediatric and neonatal patients. The limited workspace increases the risks of collisions between instruments, which can occur both inside and outside the patient. These difficulties have motivated the usage of surgical robots, such as the da Vinci Surgical System (Intuitive Surgical Inc., USA), which have been shown to improve dexterity, endurance, and vision. The da Vinci Surgical System has had great success in adult laparoscopy; however, it has been shown to be inapplicable to pediatric surgery owing to the large diameter of its instruments (8 mm) and the required in-patient length (5 cm) [2].

To provide appropriate robotic assistance to pediatric surgery and other applications in constrained workspaces,

Murilo M. Marinho, Hisashi Ishida, Kanako Harada, and Mamoru Mitsuishi are with the Department of Mechanical Engineering, the University of Tokyo, Tokyo, Japan. `Emails:{murilo, h.ishida, kanako, mamoru}@nml.t.u-tokyo.ac.jp`.

Kyoichi Deie is with the Department of Pediatric Surgery, Kitasato University Hospital, Kanagawa, Japan. `Email:kdeie@med.kitasato-u.ac.jp`

our group has been developing a novel master-slave robotic system, called SmartArm, in parallel with this work [3]. It consists of a pair of industrial robot arms, each of which is instrumented with an actuated flexible instrument [4]. The proposed system has instruments whose diameters are 3.5 mm, and the preliminary results indicate that our system can operate inside constrained workspaces, such as those in pediatric patients [5]. With the SmartArm system, we expect to bridge the gaps that prevent the wide adoption of robots in pediatric and neonate surgery [6].

As in other surgical robotics scenarios, robotic assistance in pediatric surgery may increase the task completion time owing to motion scaling as reported in the literature [7], especially when performing complex tasks. Suturing is among the most complex surgical procedures. It requires bimanual manipulation of a needle, a thread, and the target tissue. Suturing can be divided into four steps: (1) the instrument grabs the needle, (2) the needle is inserted through both sides of the tissue, (3) one of the instruments grabs the thread near the needle and loops the thread a few times around the other instrument, and finally (4) the loose end of the thread is pulled to tighten the knot. To compensate for possible robot assistance drawbacks and further improve task performance, many groups have proposed assistance methods for suturing subtasks or a combination of subtasks [8], [9], [10], [11], [7], [12].

One of those methodologies is task automation [10], [7], which has been so far demonstrated in an unobstructed space, which is not the case in pediatric endoscopy. Moreover, although the future potential of such techniques is clear, currently they are still outperformed by human-operated robots and are unable to leverage surgical skills efficiently.

In contrast, virtual fixtures do not aim to fully automate the task. Instead, virtual fixtures are used to enhance the operator's medical skills. A comprehensive survey on virtual fixtures was presented by Bowyer *et al.* [13]. The survey shows that virtual fixtures are often built using geometric elements such as points, lines, planes, and corresponding volumetric primitives. They are divided into *regional virtual fixtures*, to create a forbidden region or safe zone, and *guidance virtual fixtures*, to aid the operator in performing specific tasks.

In this letter, we focus on the generation of guidance virtual fixtures for the looping stage of suturing in an endoscopic pediatric surgery setting. Looping can be time-consuming and requires considerable skill to prevent collisions between instruments as well as with the surrounding tissues and organs. This procedure can be particularly challenging when considering the reduced workplace, the reduced haptic perception, and the

2D endoscopic vision in pediatric surgery.

A. Related works

Many studies have been conducted on the generation of guidance virtual fixtures for suturing. For instance, Kapoor *et al.* used guidance virtual fixtures to guide needle insertion [8] and in bimanual knot placement [14]. Chen *et al.* [11] introduced a knot-tying virtual fixture by constraining the tooltip to a plane. Fontanelli *et al.* [12] compared assistive methods for needle insertion and developed a guidance virtual fixture to constrain the position of the instrument along a specific trajectory while the rotations are free. Selvaggio *et al.* [15] proposed a haptic-guided shared control for needle grasping that significantly improved needle re-grasping performance. The looping task differs from needle insertion in that both instruments have to interact with each other and, especially inside the constrained workspace inside the infant, collisions have to be carefully taken into account.

To facilitate safer robot-assisted minimally-invasive partial nephrectomy, Banach *et al.* [16] proposed tool-shaft and anatomy collision avoidance using the elastoplastic frictional force control model.

Looi *et al.* [17] showed a proof of concept of a robot for image-guided anastomosis in pediatric/neonate surgery. The authors reported that the robot was able to autonomously perform sutures in some scenarios, but had difficulties in more realistic situations owing to the workspace restrictions.

In prior works, our group has focused on the generation of dynamic regional virtual fixtures to prevent collisions between instruments and to generate task constraints using vector-field inequalities [18]. More recently, we applied vector-field inequalities to teleoperation tasks and developed a unified framework for teleoperation [5]. Those works included simulations and experiments, in which the relevant task constraints were appropriately maintained. The generation of guidance virtual fixtures, i.e. specific constraints to optimize task execution, has not yet been explored using our framework.

B. Statement of contributions

In this letter, we briefly establish the benefits of the vector field inequalities (VFI) method over competing frameworks in the context of real-time virtual-fixtures generation (Section III) and propose an assistive method based on virtual fixtures to assist in the looping task in pediatric/neonatal surgery with the following components (Section IV). The proposed assistive method is evaluated in simulations and experiments with naive and expert users using an anatomically correct infant model. To the best of the authors' knowledge, this is the first work proposing guidance virtual fixtures for the looping task.

II. MATHEMATICAL BACKGROUND

In our proposed method, virtual fixtures are modeled using dual quaternion algebra and the VFI method [18] based on quadratic programming for closed-loop inverse kinematics. In this section, we briefly present the required mathematical background and notation. The proposed technique for assistance is shown in Section IV.

A. Quaternions and dual quaternions[1]

The quaternion set is $\mathbb{H} \triangleq \left\{ \boldsymbol{h} = h_1 + \hat{\imath}h_2 + \hat{\jmath}h_3 + \hat{k}h_4 : h_1, h_2, h_3, h_4 \in \mathbb{R} \right\}$, in which the imaginary units $\hat{\imath}$, $\hat{\jmath}$, and $\hat{k}$ obey $\hat{\imath}^2 = \hat{\jmath}^2 = \hat{k}^2 = \hat{\imath}\hat{\jmath}\hat{k} = -1$. Elements of the set $\mathbb{H}_p \triangleq \{\boldsymbol{p} \in \mathbb{H} : \mathrm{Re}\,(\boldsymbol{p}) = 0\}$ represent points in $\mathbb{R}^3$. The operator $\mathrm{vec}_3\,\boldsymbol{p}$ maps a $\boldsymbol{p} \in \mathbb{H}_p$ to $\mathbb{R}^3$. The set of quaternions with unit norm, $\mathbb{S}^3 \triangleq \{\boldsymbol{r} \in \mathbb{H} : \|\boldsymbol{r}\| = 1\}$, represent the rotation $\boldsymbol{r} = \cos(\phi/2) + \boldsymbol{v}\sin(\phi/2)$, where $\phi \in \mathbb{R}$ is the rotation angle around the rotation axis $\boldsymbol{v} \in \mathbb{S}^3 \cap \mathbb{H}_p$. The operator $\mathrm{vec}_4\,\boldsymbol{h}$ maps a $\boldsymbol{h} \in \mathbb{H}$ to $\mathbb{R}^4$.

The dual quaternion set is $\mathcal{H} \triangleq \left\{\underline{\boldsymbol{h}} = h + \varepsilon h' : h, h' \in \mathbb{H}, \varepsilon^2 = 0, \varepsilon \neq 0\right\}$, where ε is the dual unit. Elements of the set $\underline{\mathcal{S}} \triangleq \{\underline{\boldsymbol{x}} \in \mathcal{H} : \|\underline{\boldsymbol{x}}\| = 1\}$ represent poses $\underline{\boldsymbol{x}} = \boldsymbol{r} + \varepsilon(1/2)\boldsymbol{tr}$, where $\boldsymbol{r} \in \mathbb{S}^3$ is the rotation and $\boldsymbol{t} \in \mathbb{H}_p$ is the translation.

Elements of the set $\mathcal{H}_p \triangleq \left\{\underline{\boldsymbol{h}}_p \in \mathcal{H} : \mathrm{Re}\,(\underline{\boldsymbol{h}}) = 0\right\}$ are called pure dual quaternions and represent points ($\mathcal{H}_p \supset \mathbb{H}_p$), lines, and planes in $\mathbb{R}^3$.

Given $\underline{\boldsymbol{a}}, \underline{\boldsymbol{b}} \in \mathcal{H}_p$, their inner product and cross product are respectively $\langle \underline{\boldsymbol{a}}, \underline{\boldsymbol{b}} \rangle \triangleq -0.5\,(\underline{\boldsymbol{a}}\underline{\boldsymbol{b}} + \underline{\boldsymbol{b}}\underline{\boldsymbol{a}})$ and $\underline{\boldsymbol{a}} \times \underline{\boldsymbol{b}} \triangleq 0.5\,(\underline{\boldsymbol{a}}\underline{\boldsymbol{b}} - \underline{\boldsymbol{b}}\underline{\boldsymbol{a}})$.

A Plücker line can be written as $\underline{\boldsymbol{l}} = \boldsymbol{l} + \varepsilon\boldsymbol{m}$, where $\boldsymbol{l} \in \mathbb{H}_p \cap \mathbb{S}^3$ represents the line direction, and $\boldsymbol{m} = \boldsymbol{p_l} \times \boldsymbol{l}$ is the line moment, in which $\boldsymbol{p_l} \in \mathbb{H}_\mathbb{P}$ is a point in the line.

A plane can be written as $\underline{\boldsymbol{\pi}} \triangleq \boldsymbol{n_\pi} + \varepsilon d_\pi$, where $\boldsymbol{n_\pi} \in \mathbb{H}_p \cap \mathbb{S}^3$ is the normal to the plane, and $d_\pi = \langle \boldsymbol{p_\pi}, \boldsymbol{n_\pi} \rangle \in \mathbb{R}$.

B. Constrained optimization algorithm

Without loss of generality, the following constrained optimization algorithm can be used to teleoperate two identical slave robots R_i with $i = 1, 2$ [5]:

$$\min_{\dot{\boldsymbol{q}}} \beta \mathscr{F}_1 + (1 - \beta)\,\mathscr{F}_2 \qquad (1)$$

$$\text{subject to } \boldsymbol{W}\dot{\boldsymbol{q}} \preceq \boldsymbol{w},$$

where

$$\mathscr{F}_i \triangleq \alpha f_{t,i} + (1 - \alpha)\,f_{r,i} + f_{\Lambda,i}, \qquad (2)$$

in which $f_{t,i} \triangleq \left\| \boldsymbol{J}_{i,t}\dot{\boldsymbol{q}}_i + \eta\,\mathrm{vec}_3\,\tilde{\boldsymbol{t}}_i \right\|_2^2$, $f_{r,i} \triangleq \left\| \boldsymbol{J}_{i,r}\dot{\boldsymbol{q}}_i + \eta\,\mathrm{vec}_4\,\tilde{\boldsymbol{r}}_i \right\|_2^2$, and $f_{\Lambda,i} \triangleq \left\| \boldsymbol{\Lambda}\dot{\boldsymbol{q}}_i \right\|_2^2$ are the unweighted cost functions related to the end-effector translation, end-effector rotation, and joint velocities of the i-th robot, respectively. Furthermore, each i-th robot has a vector of joint velocities $\dot{\boldsymbol{q}}_i \in \mathbb{R}^{n_i}$, a translation Jacobian $\boldsymbol{J}_{i,t} \in \mathbb{R}^{3 \times n_i}$, a translation error $\tilde{\boldsymbol{t}}_i \triangleq \boldsymbol{t}_i - \boldsymbol{t}_{i,d} \in \mathbb{H}_p$, a rotation Jacobian $\boldsymbol{J}_{i,r} \in \mathbb{R}^{4 \times n_i}$, and a switching rotational error $\tilde{\boldsymbol{r}}_i \in \mathbb{H}_p$. In addition, $\dot{\boldsymbol{q}} = \begin{bmatrix} \dot{\boldsymbol{q}}_1^T & \dot{\boldsymbol{q}}_2^T \end{bmatrix}^T$, and $\boldsymbol{\Lambda} \in \mathbb{R}^{(n_1+n_2) \times (n_1+n_2)}$ is a positive definite damping matrix. Finally, $\alpha, \beta \in [0, 1]$ are weights used to define the priorities between the translation and the rotation and the priorities between robots. The linear constraints $\boldsymbol{W}\dot{\boldsymbol{q}} \preceq \boldsymbol{w}$ can be used to avoid joint limits [19] and to generate task constraints [18]. Each parameter is explained in more detail in [5].

---

[1]We use the notation of [18].

C. VFI method

The VFI method [18] uses a function $d \triangleq d(\boldsymbol{q}, t) \in \mathbb{R}$ that represents the (signed) distance between two geometric primitives. The time-derivative of the distance is

$$\dot{d} = \underbrace{\frac{\partial\left(d(\boldsymbol{q}, t)\right)}{\partial \boldsymbol{q}}}_{\boldsymbol{J}_d} \dot{\boldsymbol{q}} + \zeta(t), \qquad (3)$$

where $\boldsymbol{J}_d \in \mathbb{R}^n$ is the distance Jacobian and $\zeta(t) = \dot{d} - \boldsymbol{J}_d\dot{\boldsymbol{q}}$ is the residual. Moreover, let there be a safe distance $d_{\text{safe}} \triangleq d_{\text{safe}}(t) \in [0, \infty)$ and an error $\tilde{d} \triangleq \tilde{d}(\boldsymbol{q}, t) = d - d_{\text{safe}}$ to generate restricted zones or $\tilde{d} \triangleq d_{\text{safe}} - d$ to generate safe zones.

With these definitions, and given $\eta_d \in [0, \infty)$, the signed distance dynamics is constrained by $\dot{\tilde{d}} \geq -\eta_d \tilde{d}$, which actively filters the robot motion only in the direction approaching the restricted zone boundary so that the primitives do not collide.

The following constraint is used to generate restricted zones

$$-\boldsymbol{J}_d\dot{\boldsymbol{q}} \leq \eta_d\tilde{d} + \zeta_{\text{safe}}(t), \qquad (4)$$

for $\zeta_{\text{safe}}(t) \triangleq \zeta(t) - \dot{d}_{\text{safe}}$. Alternatively, safe zones are generated by

$$\boldsymbol{J}_d\dot{\boldsymbol{q}} \leq \eta_d\tilde{d} - \zeta_{\text{safe}}(t). \qquad (5)$$

1) Generating an entry sphere using VFIs: As an example relevant to the application of this letter, in infant surgery, instead of an entry-point constraint, an entry-sphere constraint is used [5]. This constraint replicates the manual technique of medical doctors that utilizes the compliance of the infant's skin to increase the reachable workspace. To generate this constraint, without loss of generality, let $\underline{\boldsymbol{x}}_i = \boldsymbol{r}_i + \varepsilon\frac{1}{2}\boldsymbol{t}_i\boldsymbol{r}_i$ be a coordinate frame whose $z-$axis is along the shaft of the instrument of a given robot R_i. The Plücker line associated with the instrument shaft's axis, $\underline{\boldsymbol{l}}_{z,i}\underline{\mathcal{S}}$, can be expressed by

$$\underline{\boldsymbol{l}}_{z,i} = \boldsymbol{l}_{z,i} + \varepsilon\boldsymbol{m}_{z,i} \qquad (6)$$

in which $\boldsymbol{l}_{z,i} = \boldsymbol{r}_i\hat{k}\boldsymbol{r}_i^* \in \mathbb{H}_p \cap \mathbb{S}^3$ is the line direction and $\boldsymbol{m}_{z,i} = \boldsymbol{t}_i \times \boldsymbol{l}_{z,i} \in \mathbb{H}_p$ is the line moment. With the center of the entry sphere given by $\boldsymbol{p}_{\text{rcm},i} \in \mathbb{H}_p$, the derivative of the squared distance between the entry point and the instrument's shaft is given by

$$\dot{D}_{\text{rcm},i} = \boldsymbol{J}_{l_{z,i},p}\dot{\boldsymbol{q}}_i, \qquad (7)$$

where $\boldsymbol{J}_{l_{z,i},p} \in \mathbb{R}^{n_i}$ is the line-to-point squared distance Jacobian [18]. Using the VFI method, the instrument's shaft can be constrained by an entry sphere of squared radius $D_{\text{safe,rcm,i}} \in \mathbb{R}$ by using the following linear constraint:

$$\underbrace{\boldsymbol{J}_{l_{z,i},p}\dot{\boldsymbol{q}}_i}_{\boldsymbol{W}_{\text{rcm}}} \leq \underbrace{\eta_{\text{rcm},i}(D_{\text{safe,rcm},i} - D_{\text{rcm},i})}_{\boldsymbol{w}_{\text{rcm}}}, \qquad (8)$$

where $\eta_{rcm,i} \in [0, \infty)$ is a gain that affects the allowed speed of the instrument's shaft toward the surface of the sphere.
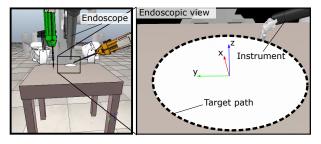

Fig. 1. The V-REP simulation used in the simulation comparison. The circle's z-axis position changed in time following a sinusoidal wave $d(t) = d_o + 0.01\sin\left(2\pi 0.1t\right)$.

III. WHY VFI?

There are myriad of competing techniques for the generation of virtual fixtures/active constraints [13]. For nonredundant robots, such as the da Vinci, virtual fixtures based on force feedback on the master side are effective [20], [13], [16]. For redundant robots, such as the SmartArm and similar systems, only force feedback on the master side is in general not enough, owing to possibly infinite mappings between master and slave postures. That is, with unconstrained inverse kinematics, pushing the master in a given direction, in general, *does not guarantee* that a redundant slave's links will move in a repeatable manner. This problem becomes more evident in surgeries in constrained spaces such as pediatric and neonate surgery. In this context, we have been developing a framework [5] based on active constraints generated through constrained optimization on the slave side, which *guarantees* the integrity of the robotic systems and the safety of the patients and operating room personnel. On the master side, we add Cartesian impedance to make the operator aware of the workspace constraints.

To validate the benefits of the VFI method over existing works, we show a brief simulation study.

In the existing literature, active constraints using constrained optimization in the context of robotic surgery were initially proposed by Kapoor *et al.* [9]. They proposed several primitives that can be used to assemble customizable virtual fixtures, and one of their primitives in common with the VFI method is the plane constraint. In this context, we compare the performance of the constraint proposed in [9] with what can be achieved with VFIs. Because there is no explicit objective function for teleoperation in [9], we used the same objective function (with the same gains) for both methods and changed only the constraints.

To compare both techniques, we used the V-REP simulation developed in [12]. A suitable scenario using the plane constraint common to both techniques is to require the robots' tooltips to be restricted to a dynamic plane while the robot is teleoperated. The dynamic-plane distance changes in a sinusoidal manner along the z-axis according to $d(t) = d_o + 0.01\sin\left(2\pi 0.1t\right)$ with a fixed normal.

The user was asked to trace, by using the master interface, a circle seen through the simulated endoscope. The experiment was performed once without any plane motion, and that trajectory was recorded and played back for each technique to ensure that the trajectory on the xy-plane was the same for all cases. To further increase the difficulty of the task, the

tooltip starts 30 mm away from the dynamic plane.

The tooltip distance with respect to the plane for each method is shown in Fig. 2. A considerable deviation from the plane, 5.27 mm, was observed when using the constraints proposed in [9]. This occurred because the constraint proposed in [9] does not take into account the instantaneous velocity of the plane; therefore, there was a steady-state offset between the desired plane and the actual plane. When VFIs were used, the residual (as shown in (3)) acted as a feed-forward term that compensated for the plane's instantaneous velocity, which allowed convergence to the moving plane.

This property is required for the proper generation of dynamic virtual fixtures such as the ones proposed in this letter.
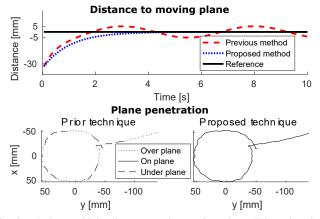

Fig. 2. Robot tooltip's distance to the moving plane. When the plane constraint is defined by using the prior technique [9], the tooltip considerable deviates from the plane. Using our proposed technique, the tooltip converges to the moving plane and moves with it.

IV. PROPOSED ASSISTIVE METHOD FOR SUTURING

The proposed assistive method for suturing is divided into two parts: a constrained optimization algorithm on the slave side (Section IV-B) and Cartesian impedance feedback on the master side (Section IV-C).
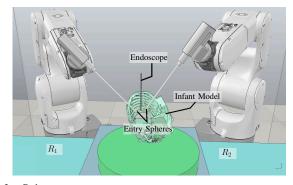
A. Problem statement

Fig. 3. Robot setup.

Consider the setup shown in Fig. 3. Let there be two robots, R_1 and R_2, with instruments as their end effector. Suppose that the instruments can be simplified as capsules (cylinders

with spheres on their endpoints). For robot-aided endoscopic infant surgery, each instrument has to be inserted through the intercostal space (between the ribs) of the infant. Each incision on the skin cannot be pushed, to prevent further damage to the tissue. This is accomplished by adding an entry-sphere constraint for each robot, as discussed in Section II-C1.

One of the required steps in suturing is to loop the thread about one of the instruments before grasping the loose end of the thread and tying the knot. In this step, the inexperienced user can loop too far (risking collisions with the anatomy) or too close (risking collisions with the other instrument). The proposed technique, described in the following sections, aims to assist the surgeon in performing the looping in a safer and more controlled manner.

B. Slave side: Constrained optimization

Let R_1 be the slave robot operated by the non-dominant hand, and R_2 be the robot operated by the dominant hand. In this work, we propose a set of dynamic virtual fixtures attached to R_1 that constrain the motion of R_2 to aid the robotic thread looping task in suturing. The proposed virtual fixtures have been designed by careful inspection of videos of medical practice in pediatric surgery [21] and fruitful discussions with cooperating surgeons. We make two basic assumptions. First, restricting the motion of one instrument with respect to the other using virtual fixtures during the looping task to a guidance region can be helpful in reducing extraneous motion. Second, adding a guidance surface can further improve task performance.

The dynamic virtual fixtures, which we call looping virtual fixtures (LVFs), are generated by employing a shaft—shaft collision avoidance primitive [18] plus three geometric primitives for the tooltip of R_1. First, we attach a dynamic cylinder $c_{\max}$ with a radius of $r_{\max}$ around the $z-$axis of the end effector of R_1

$$\underline{l}_{z,1} = \overbrace{r_1 \hat{k} r_1^*}^{l_{z,1}} + \varepsilon \left(t_1 \times l_{z,1} \right) \tag{9}$$

in which $r_1 \in \mathbb{S}^3$ and $t_1 \in \mathbb{H}_p$ are respectively the rotation and translation of R_1. The cylinder is cut with a pair of planes $\pi_{\min}$ and $\pi_{\max}$ whose normals are collinear with $\underline{l}_{z,1}$ and are respectively placed at $d_{\pi,\min}$ and $d_{\pi,\max}$ from the tooltip of R_1

$$\pi_{\min} \triangleq n_\pi + \varepsilon \left(\langle t_1, n_\pi \rangle + d_{\pi,\min} \right) \tag{10}$$

$$\pi_{\max} \triangleq n_\pi + \varepsilon \left(\langle t_1, n_\pi \rangle + d_{\pi,\max} \right) \tag{11}$$

in which $n_\pi = r_1 \hat{k} r_1^*$. These geometric constraints, shown in Fig. 4, limit the motion of R_2 so that its tooltip is constrained within a motion envelope to prevent large motions that can be detrimental to task performance, as well as preventing collisions between the shafts and the surrounding tissues. The radius of the cylinder and the placement of the planes can be tuned to balance loop size and task performance.

The LVF can be generated using linear constraints by employing VFIs. With the shaft-shaft collision avoidance given by [18, Eq. 64]

$$W_{ss} \leq w_{ss}, \tag{12}$$
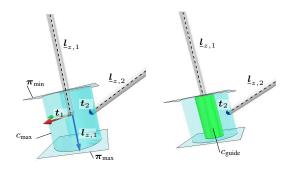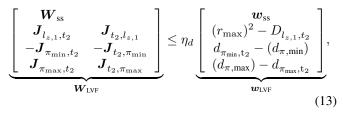
Fig. 4. Visualization of LVFs (left) and TGC (right).

the LVFs can be generated by the following linear constraints

$$
\underbrace{\begin{bmatrix} \boldsymbol{W}_{\mathrm{ss}} \\ \boldsymbol{J}_{l_{z,1},t_2} & \boldsymbol{J}_{t_2,l_{z,1}} \\ -\boldsymbol{J}_{\pi_{\min},t_2} & -\boldsymbol{J}_{t_2,\pi_{\min}} \\ \boldsymbol{J}_{\pi_{\max},t_2} & \boldsymbol{J}_{t_2,\pi_{\max}} \end{bmatrix}}_{\boldsymbol{W}_{\mathrm{LVF}}} \leq \eta_d \underbrace{\begin{bmatrix} \boldsymbol{w}_{\mathrm{ss}} \\ (r_{\max})^2 - D_{l_{z,1},t_2} \\ d_{\pi_{\min},t_2} - (d_{\pi,\min}) \\ (d_{\pi,\max}) - d_{\pi_{\max},t_2} \end{bmatrix}}_{\boldsymbol{w}_{\mathrm{LVF}}},
$$

(13)

in which $\boldsymbol{J}_{l_{z,1},t_2}$ is the line-to-point distance Jacobian [18, Eq. 34] between the Plücker line collinear with the shaft of R_1, $\underline{\boldsymbol{l}}_{z,1}$, and the tooltip of R_2, $\boldsymbol{t}_2$. Moreover, $\boldsymbol{J}_{t_2,l_{z,1}}$ is the point-to-line distance Jacobian [18, Eq. 32] between $\underline{\boldsymbol{l}}_{z,1}$ and $\boldsymbol{t}_2$. Furthermore, $\boldsymbol{J}_{\pi_{\min},t_2}$ and $\boldsymbol{J}_{\pi_{\max},t_2}$ are plane-to-point distance Jacobians [18, Eq. 56] between $\pi_{\min}$ and $\boldsymbol{t}_2$, and $\pi_{\max}$ and $\boldsymbol{t}_2$, respectively. Conversely, $\boldsymbol{J}_{t_2,\pi_{\min}}$ and $\boldsymbol{J}_{t_2,\pi_{\max}}$ are the point-to-plane distance Jacobians [18, Eq. 59] between $\pi_{\min}$ and $\boldsymbol{t}_2$, $\pi_{\max}$ and $\boldsymbol{t}_2$, respectively. $D_{l_{z,1},t_2}$ is the line-to-point squared distance [18, Eq. 33] between $\underline{\boldsymbol{l}}_{z,1}$ and $\boldsymbol{t}_2$. Lastly, $d_{\pi_{\min},t_2}$ and $d_{\pi_{\max},t_2}$ are the plane-to-point distances [18, Eq. 54] between $\pi_{\min}$ and $\boldsymbol{t}_2$, and $\pi_{\max}$ and $\boldsymbol{t}_2$, respectively.

To further increase assistance, we propose a guidance virtual fixture, called trajectory guidance cylinder (TGC). It comprises a cylinder c_{guide} with its centerline collinear to $\underline{\boldsymbol{l}}_{z,1}$ and radius r_{guide} that is placed inside the LVFs and used to guide the tooltip of R_2.

We propose the following constrained optimization problem to implement both the LVFs and the TGC

$$
\min_{\dot{\boldsymbol{q}}} \ \gamma(\mathscr{F}_1 + \mathscr{F}_2) + (1-\gamma)(\mathscr{G}_1 + \mathscr{G}_2) + (f_{\Lambda,1} + f_{\Lambda,2})
$$

$$
\text{subject to } \boldsymbol{W}\dot{\boldsymbol{q}} \preceq \boldsymbol{w}, \quad (14)
$$

where $\mathscr{F}_i$ is related to trajectory tracking as in (1) and $\mathscr{G}_i$ is related to the TGC of the i-th robot as follows

$$
\mathscr{G}_1 \triangleq \boldsymbol{J}_{l_{z,1},t_2}\dot{\boldsymbol{q}}_1 + \eta_{\mathrm{guide}}\tilde{D}_{\mathrm{guide}} \quad (15)
$$

$$
\mathscr{G}_2 \triangleq \boldsymbol{J}_{t_2,l_{z,1}}\dot{\boldsymbol{q}}_2 + \eta_{\mathrm{guide}}\tilde{D}_{\mathrm{guide}}, \quad (16)
$$

where the guidance error is defined as $\tilde{D}_{\mathrm{guide}} \triangleq D_{l_{z,1},t_2} - r_{\mathrm{guide}}^2$. Lastly, $\alpha, \gamma \in [0,1]$ are, respectively, weights used to define the priorities between the translation and the rotation and between the master-slave tracking and the TGC. The linear constraints are given by

$$
\overbrace{\begin{bmatrix} \boldsymbol{W}_{\mathrm{JL}} \\ \boldsymbol{W}_{\mathrm{rcm}} \\ \boldsymbol{W}_{\mathrm{LVF}} \end{bmatrix}}^{\boldsymbol{W}} \leq \overbrace{\begin{bmatrix} \boldsymbol{w}_{\mathrm{JL}} \\ \eta_{\mathrm{rcm}}\boldsymbol{w}_{\mathrm{rcm}} \\ \eta_d\boldsymbol{w}_{\mathrm{LVF}} \end{bmatrix}}^{\boldsymbol{w}}, \quad (17)
$$

in which $\boldsymbol{W}_{\mathrm{JL}} \leq \boldsymbol{w}_{\mathrm{JL}}$ is related to joint limit avoidance [19], $\boldsymbol{W}_{\mathrm{rcm}} \leq \boldsymbol{w}_{\mathrm{rcm}}$ is related to the entry-sphere constraint as in (8), and finally $\boldsymbol{W}_{\mathrm{LVF}} \leq \boldsymbol{w}_{\mathrm{LVF}}$ as defined in (13).

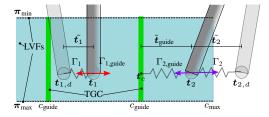*C. Master side: Cartesian impedance with guidance*

Fig. 5. Visualization of the Cartesian impedance from the point-of-view of the slave robots. The blue region is the safe region enveloped by the LVFs and the green line represents the TGC. The forces Γ_1, Γ_2, $\Gamma_{1,\mathrm{guide}}$, and $\Gamma_{2,\mathrm{guide}}$ are calculated based on the slave-side errors, projected to the master side, and applied at the master interfaces according to (18) and (19). The guidance error is $\tilde{\boldsymbol{t}}_{\mathrm{guide}} \triangleq \boldsymbol{t}_2 - \boldsymbol{t}_c$ in which $\boldsymbol{t}_c$ is the translation of the point in c_{guide} closest to $\boldsymbol{t}_2$.

In addition to the existing method of Cartesian force feedback introduced in [5], we propose additional force feedback to guide the tooltip of R_2 to the cylinder c_{guide} in the form

$$
\boldsymbol{\Gamma}_{1,\mathrm{total}}^{\mathrm{master}} \triangleq \overbrace{-\eta_f\gamma\tilde{\boldsymbol{t}}_1^{\mathrm{master}}}^{\Gamma_1^{\mathrm{master}}} \overbrace{-\eta_f(1-\gamma)\tilde{\boldsymbol{t}}_{\mathrm{guide}}^{\mathrm{master}}}^{\Gamma_{1,\mathrm{guide}}^{\mathrm{master}}} -\eta_V\dot{\boldsymbol{t}}_{1,\mathrm{master}}^{\mathrm{master}}, \quad (18)
$$

$$
\boldsymbol{\Gamma}_{2,\mathrm{total}}^{\mathrm{master}} \triangleq \underbrace{-\eta_f\gamma\tilde{\boldsymbol{t}}_2^{\mathrm{master}}}_{\Gamma_2^{\mathrm{master}}} \underbrace{+\eta_f(1-\gamma)\tilde{\boldsymbol{t}}_{\mathrm{guide}}^{\mathrm{master}}}_{\Gamma_{2,\mathrm{guide}}^{\mathrm{master}}} -\eta_V\dot{\boldsymbol{t}}_{2,\mathrm{master}}^{\mathrm{master}}. \quad (19)
$$

For each i-th robot master–slave pair, $\boldsymbol{\Gamma}_{i,\mathrm{total}}^{\mathrm{master}}$ is the force on the i-th master and $\eta_f, \eta_V \in (0,\infty)$ are stiffness and viscosity parameters. $\tilde{\boldsymbol{t}}_i^{\mathrm{master}}$ is the translation error of the i-th slave seen from the point of view of the master,[2] and $\dot{\boldsymbol{t}}_{i,\mathrm{master}}^{\mathrm{master}}$ is the linear velocity of the i-th master interface. $\tilde{\boldsymbol{t}}_{\mathrm{guide}}^{\mathrm{master}}$ is the guidance error of the slaves from the point of view of the master. Finally, $\gamma \in [0,1]$ is used to define the priority between the master-slave tracking force feedback, $\Gamma_i^{\mathrm{master}}$, and the TGC force feedback, $\Gamma_{i,\mathrm{guide}}^{\mathrm{master}}$. Those two forces act as a spring, trying to reduce the tracking and guidance errors, as shown in Fig. 5.

V. SIMULATION AND EXPERIMENT

To evaluate the technique proposed in this paper, we designed a simulation study and an experimental study. The simulation entailed naive users operating a simulator (V-REP, Coppelia Robotics, Switzerland) under three different conditions to evaluate the effects of the proposed technique. The experimental study investigated medical doctors' performance using the proposed technique while operating a robotic system [22] based on the SmartArm architecture [3], with a two degrees-of-freedom (rotation, grasping) instrument attached, in a setup equivalent to [5].

The experimental setup is shown in Fig. 6. The 3D model of an infant [21] (Fig. 7) was placed between the two robotic

---

[2]The point-of-view of the master is the point-of-view of the endoscopic camera.

arms, and the entry spheres (Section II-C1) were placed between the ribs of the infant model at their relevant locations. In these experiments, the two robotic arms (DENSO VS050, DENSO WAVE Inc., Japan) were equipped with rigid 3.5-mm-diameter instruments. The simulator replicated the experimental setup.
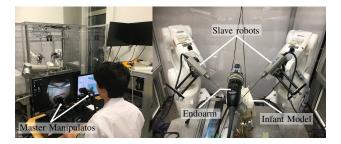

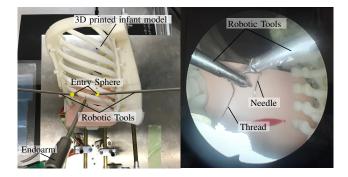Fig. 6. Master–slave robotic system. Master-side (*left*), slave-side (*right*).

Fig. 7. Experimental Setup. Top view of the 3D printed infant model [2] (*left*) and endoscopic view (*right*).

Both the simulation and the experiment used the same software implementation described in [3].

All p values reported in this section were obtained through the (two-tailed) Wilcoxon signed-rank task.

TABLE I
CONTROL PARAMETERS AND VIRTUAL FIXTURE PARAMETERS.

α	β	γ	η	η_d	η_{rcm}	η_{guide}	Λ	η_f	η_V	MS
0.999	0.6	0.01	150	30	30	1	0.02	50	0.5	1/2

r_{min}	r_{max}	r_{guide}	$d_{safe,rcm}$	$d_{\pi,min}$	$d_{\pi,max}$
3.5	20	10	2.5	-8	10

α: translation error to orientation error weight (Section II-B).
β: robot priority weight (Section II-B)
γ: weights between the master-slave tracking and TGC (Section IV-B).
η, η_d,η_{guide}: proportional gain of the kinematic controller, LVF, and TGC, respectively.
Λ: Robot joint gains (Section II-B).
η_F, η_V: Cartesian impedance proportional and viscosity gains, respectively (Section IV-C).
MS: Motion scaling. A motion scaling of X means that a relative translation of the master was multiplied by X before being sent to the slave.
$r_{min}, r_{max}, r_{guide}, d_{safe,rcm}, d_{\pi,min}, d_{\pi,max}$ virtual fixture parameters in millimeters (Section IV-B).

A. Simulation

For the simulation study, six volunteers were recruited among the engineering students at the University of Tokyo, who had no medical experience. After being shown a video

demonstrating the ideal double loop trajectory, the users were instructed to replicate that loop as closely as possible. Each user was asked to perform in the simulator a double loop in a total of five trials in each of the following three conditions: A1 with only the entry-sphere constraint (control group), A2 with the entry-sphere constraint and the shaft–shaft collision avoidance (first mentioned in [18]), and A3 with the entry-sphere constraint and the proposed LVFs and TGC.

The trials were done using a replicated balanced Latin-squares design [23] with the trials and users as blocking factors. Each user performed a total of 15 trials. To reduce possible biases, the users did not know which condition was activated at a given trial. The proposed virtual fixtures were implemented using (14) and were determined by pilot studies overseen by a medical doctor. Their relevant parameters are shown in Table I.

The simulation had two purposes. First, to evaluate the effectiveness of the proposed technique with inexperienced users. Second, to investigate condition A1, which has no virtual fixtures to prevent collisions between shafts; therefore, we could investigate collisions between instruments and the anatomical model without damaging the physical equipment. It is important to note that the surgical thread was not simulated; only the loop motion was evaluated.

1) Results and discussion:

a) Controller performance: To evaluate the performance of the looping task, we used the task completion time and the error between the tooltip position of R_2 and the surface of the guidance cylinder (Section IV-B) that delineates the ideal looping surface. Table II shows the median time and mean error recorded for the six volunteers for each of the three experimental cases.

TABLE II
USER PERFORMANCE IN THE SIMULATION.

	A1	A2	A3
Median time [s]	14.56	17.12	17.10
Mean error [mm]	2.267	1.261	1.211

For A1, the users took a median of 14.56 s to complete the task. That was the shortest completion time between all experimental conditions ($p < 0.05$). However, the mean trajectory error was the highest and, as expected, there were collisions between the instruments.

A2 provided a collision-free path for the instruments and a 44% reduction in the mean trajectory error with respect to A1. There was a 18% increase ($p < 0.05$) in the median required time with respect to A1.

Finally, after adding the proposed guidance virtual fixtures, in condition A3 the instrument path was also collision-free. Moreover, there was a reduction of 4% in the mean trajectory error with respect to A2 (47% with respect to A1). There was no reduction in the median time with respect to A2 (17% increase with respect to A1 ($p < 0.05$)).

These results show that our proposed method, A3, is equivalent to A2 in terms of controller performance. It is slightly superior in terms of mean trajectory error.

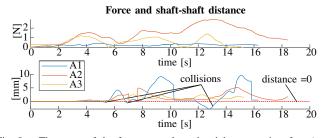A sample of the force rendered on the right master for each condition is shown in Fig. 8.

Fig. 8. The norm of the force exerted on the right master interface (*top*) and the signed distance between shafts (*bottom*) for one double-looping trial under each condition on the simulation study. Only condition A1 had collisions between shafts.

b) User evaluation: The users were asked to complete the NASA TLX workload survey [24] to evaluate the workload in terms of six indicators: *mental demand*, *physical demand, temporal demand, performance, effort*, and *frustration*. The results of the survey are shown in Fig. 9. We normalized the scores of the NASA TLX to compare the relative scores between techniques. The sum of the NASA TLX indicators for each condition were 80.1 (for A1), 56.6 (for A2), 46.73 (for A3) out of 126.
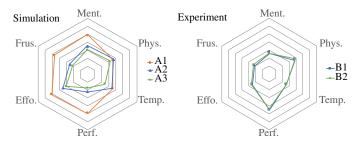

Fig. 9. NASA TLX workload survey in three conditions for the simulation (*left*) and in two conditions for the experiment (*right*). Conditions are as follows: A1: with no virtual fixtures (only the entry-sphere constraint), A2, B1: with shaft-shaft collision avoidance, A3, B2: with both LVFs and TGC. Values near the center indicate better results.

Comparing A1 with A2, A1 had the highest workload when summing up all indicators ($p < 0.05$). In special, A1 had a highest score in *mental demand* ($p < 0.05$), *performance* ($p < 0.05$), *frustration* ($p < 0.05$), and *effort* ($p < 0.05$). There was no statistical significance in *physical demand* ($p = 0.84$) and *temporal demand* ($p = 0.69$). From the feedback we received from the users, operating the system without the automatic constraints increased their overall workload because they had to prevent collisions while performing the looping task manually.

Comparing A2 with A3, A3 had the lowest sum of workload indicators ($p < 0.05$). A3 significantly reduced the *physical demand* ($p < 0.05$) and *temporal demand* ($p < 0.05$) during the looping motion. There was no significant difference in *mental demand* ($p = 0.07$), *performance* ($p = 0.06$), *effort* ($p = 0.06$), and *frustration* ($p = 0.18$).

These results show that, in terms of workload, A3 was the superior technique overall.

In addition to the workload survey, the users were asked "What was your biggest difficulty with the system/what as-pects of the system could be improved?" as an open-ended question. Two comments regarded the tunning of the system "the motion scaling is too small" and "the tools move too fast," which might be addressed by a user-specific system tunning in future works. In addition, some difficulties were specific to the task itself "depth was hard to perceive" because of the 2D images, and "the RCM constraint was the major cause of inconvenience."

B. Experiment

The experiment was designed to study the effect of the proposed methods on the medical doctors during a robot-aided surgical looping. The experimental setup replicated the simulation, and the experimental parameters are shown in Table I. A surgical thread (5-0 PERMA-HAND SILK, ETHICON, USA) was held by the robot controlled by the operator's dominant hand. In this experiment, the base of the robots and the tooltip position with respect to the robotic end-effector were calibrated by using a visual-tracking system (Polaris Spectra, NDI, Canada) through a pivoting process [18].

Two pediatric surgeons, one expert level (EL) and one intermediate level (IL), were recruited. The surgeons were instructed to perform the double loop under two conditions: B1 only with shaft–shaft collision avoidance and B2 with both LVFs and TGC. The double loop was performed 10 times, 5 times for each condition. The users operated the robots using the haptic interfaces, and the images captured by the endoscope (Endoarm, Olympus, Japan) were displayed on a monitor. All the conditions were assigned in random a sequence to reduce possible biases.

1) Results and discussion:

a) Controller performance: The medical doctors suc-cessfully conducted the surgical looping under both condi-tions, *i.e.,* they looped the surgical thread twice about the left instrument, and those loops were stable. In addition, no collisions happened. The task completion time and the error between the tooltip of R_2 and the surface of the guidance cylinder (Section IV-B) were recorded during the experiment. The results are shown in Table. III.

For the median task completion time for conditions B1 and B2, there was no significant difference for the EL ($p = 0.875$) and the IL ($p = 0.32$). The median task completion time for the IL appears skewed towards a reduction of task completion time when using the guidance virtual fixtures in condition B2.

The error between the R_2 tooltip and the guidance cylinder decreased by an average of 33% for the EL and by 11% for the IL. These results indicate that the virtual fixtures decreased the error more for the EL than for the IL. We conjecture that the more substantial reduction of error for the EL might be related to how the EL operated the master interface. The EL moved the master interfaces more softly than the IL, giving more room for the virtual fixtures to assist and decrease the error.

These results indicate benefits for medical doctors as well, but more users will be required in follow-up studies to investigate this hypothesis further.

TABLE III
USER PERFORMANCE IN THE EXPERIMENT.

	Expert		Intermediate		Total	
	B1	B2	B1	B2	B1	B2
Median time [s]	33	32	31.5	28	32	31
Mean error [mm]	0.89	0.59	2.16	1.92	1.82	1.40

b) User evaluation: The surgeons completed the same modified NASA TLX survey, and there was no significant difference ($p > 0.25$) in the workload between B1 and B2 (Fig. 9). These results indicate that the proposed method successfully guided the instruments closer to the desired surface without a noticeable difference in the workload felt by the surgeon.

In the experimental study, we could observe a collision-free looping with decreased overall looping error. This assistance is essential when the medical doctors are learning how to use the robotic system (even if they are experienced in manual surgery), to prevent damage to the instruments and the anatomical model. A more comprehensive experimental study with a larger number of surgical doctors is required in follow-up studies to investigate at which point in their learning curve the medical doctors can most benefit from the proposed assistance method.

VI. CONCLUSIONS

In this paper, two virtual fixtures for looping were proposed, the looping virtual fixtures (LVFs) and the trajectory guidance cylinder (TGC). These methods can improve the safety and precision of the looping task in surgical suturing under the constrained workspace of pediatric surgery. On the slave side, a constrained optimization algorithm generates the LVFs and the TGC. On the master side, a Cartesian impedance algorithm allows the user to "feel" safe directions (LVFs) and optimal directions (TGC) during the looping. The proposed algorithm is evaluated in a simulation and an experiment with users that show the safety and increased precision of the looping. The results of our simulation study indicate that the proposed methods might be more effective when used by operators with less experience.

REFERENCES

[1] T. P. Cundy, H. J. Marcus, A. Hughes-Hallett, T. MacKinnon, A. S. Najmaldin, G.-Z. Yang, and A. Darzi, "Robotic versus non-robotic instruments in spatially constrained operating workspaces: a pre-clinical randomized crossover study," *BJU International*, vol. 116, no. 3, pp. 415–422, may 2015.

[2] S. Takazawa, T. Ishimaru, K. Harada, K. Deie, A. Hinoki, H. Uchida, N. Sugita, M. Mitsuishi, T. Iwanaka, and J. Fujishiro, "Evaluation of surgical devices using an artificial pediatric thoracic model: A comparison between robot-assisted thoracoscopic suturing versus conventional video-assisted thoracoscopic suturing," *Journal of Laparoendoscopic & Advanced Surgical Techniques*, vol. 28, no. 5, pp. 622–627, may 2018.

[3] M. M. Marinho, K. Harada, A. Morita, and M. Mitsuishi, "Smartarm: Integration and validation of a versatile surgical robotic system for constrained workspaces," *The International Journal of Medical Robotics and Computer Assisted Surgery (IJMRCAS)*, 2019, (in press).

[4] J. Arata, Y. Fujisawa, R. Nakadate, K. Kiguchi, K. Harada, M. Mitsuishi, and M. Hashizume, "Compliant four degree-of-freedom manipulator with locally deformable elastic elements for minimally invasive surgery," in *2019 International Conference on Robotics and Automation (ICRA)*. IEEE, May 2019.

[5] M. M. Marinho, B. V. Adorno, K. Harada, K. Deie, A. Deguet, P. Kazanzides, R. H. Taylor, and M. Mitsuishi, "A unified framework for the teleoperation of surgical robots in constrained workspaces," in *2019 International Conference on Robotics and Automation (ICRA)*. IEEE, may 2019.

[6] T. P. Cundy, H. J. Marcus, A. Hughes-Hallett, S. Khurana, and A. Darzi, "Robotic surgery in children: adopt now, await, or dismiss?" *Pediatric Surgery International*, vol. 31, no. 12, pp. 1119–1125, Sep. 2015.

[7] T. Osa, N. Sugita, and M. Mitsuishi, "Online trajectory planning and force control for automation of surgical tasks," *IEEE Transactions on Automation Science and Engineering*, vol. 15, no. 2, pp. 675–691, Apr. 2018.

[8] A. Kapoor, M. Li, and R. H. Taylor, "Spatial motion constraints for robot assisted suturing using virtual fixtures," in *International Conference on Medical Image Computing and Computer-Assisted Intervention*. Springer, May 2005, pp. 89–96.

[9] ——, "Constrained control for surgical assistant robots." in *2006 International Conference on Robotics and Automation (ICRA)*, May 2006, pp. 231–236.

[10] S. Sen, A. Garg, D. V. Gealy, S. McKinley, Y. Jen, and K. Goldberg, "Automating multi-throw multilateral surgical suturing with a mechanical needle guide and sequential convex optimization," in *2016 IEEE International Conference on Robotics and Automation (ICRA)*. IEEE, May 2016.

[11] Z. Chen, A. Malpani, P. Chalasani, A. Deguet, S. S. Vedula, P. Kazanzides, and R. H. Taylor, "Virtual fixture assistance for needle passing and knot tying," in *IEEE/RSJ International Conference on Intelligent Robots and Systems (IROS)*. IEEE, Oct. 2016, pp. 2343–2350.

[12] G. A. Fontanelli, G.-Z. Yang, and B. Siciliano, "A comparison of assistive methods for suturing in MIRS," in *2018 IEEE/RSJ International Conference on Intelligent Robots and Systems (IROS)*. IEEE, oct 2018.

[13] S. A. Bowyer, B. L. Davies, and F. R. y Baena, "Active constraints/virtual fixtures: A survey," *IEEE Transactions on Robotics*, vol. 30, no. 1, pp. 138–157, 2014.

[14] A. Kapoor and R. H. Taylor, "A constrained optimization approach to virtual fixtures for multi-handed tasks," in *2008 International Conference on Robotics and Automation (ICRA)*. IEEE, may 2008.

[15] M. Selvaggio, A. Ghalamzan, R. Moccia, F. Ficuciello, and B. Siciliano, "Haptic-guided shared control for needle grasping optimization in minimally invasive robotic surgery," in *2019 IEEE/RSJ International Conference on Intelligent Robots and Systems (IROS)*, Nov. 2019.

[16] A. Banach, K. Leibrandt, M. Grammatikopoulou, and G.-Z. Yang, "Active constraints for tool-shaft collision avoidance in minimally invasive surgery," in *2019 International Conference on Robotics and Automation (ICRA)*. IEEE, May 2019.

[17] T. Looi, B. Yeung, M. Umasthan, and J. Drake, "KidsArm an image-guided pediatric anastomosis robot," in *2013 IEEE/RSJ International Conference on Intelligent Robots and Systems*. IEEE, Nov. 2013.

[18] M. M. Marinho, B. V. Adorno, K. Harada, and M. Mitsuishi, "Dynamic active constraints for surgical robots using vector-field inequalities," *IEEE Transactions on Robotics*, vol. 35, no. 5, pp. 1166–1185, oct 2019.

[19] F.-T. Cheng, T.-H. Chen, and Y.-Y. Sun, "Resolving manipulator redundancy under inequality constraints," *IEEE Transactions on Robotics and Automation*, vol. 10, no. 1, pp. 65–71, Feb 1994.

[20] S. A. Bowyer and F. R. y Baena, "Dynamic frictional constraints for robot assisted surgery," in *World Haptics Conference (WHC), 2013*. IEEE, 2013, pp. 319–324.

[21] K. Harada, G. Ishikawa, S. Takazawa, T. Ishimaru, N. Sugita, T. Iwanaka, and M. Mitsuishi, "Development of a neonatal thoracic cavity model and preliminary study," *Journal of Japan Society of Computer Aided Surgery*, vol. 18, no. 2, pp. 80–86, 2016.

[22] S. Kim, J. L. Buendia, S. A. Heredia-Perez, M. M. Marinho, K. Harada, N. Kaneko, T. Ushiku, and M. Mitsuishi, "Towards the automation of grossing in pathology examinations using industrial robotic arms," in *The 14th Asian Conference on Computer Aided Surgery (ACCAS)*, Nov. 2018, pp. 202–203.

[23] E. Williams, "Experimental designs balanced for the estimation of residual effects of treatments," *Australian Journal of Chemistry*, vol. 2, no. 2, pp. 149–168, 1949.

[24] S. G. Hart, "Nasa-task load index (NASA-TLX) 20 years later," *Proceedings of the Human Factors and Ergonomics Society Annual Meeting*, vol. 50, no. 9, pp. 904–908, oct 2006.